

## Article

# Assessment of Narrow Band Imaging Algorithm for Video Capsule Endoscopy Based on Decorrelated Color Space for Esophageal Cancer

Kai-Yao Yang<sup>1,†</sup>, Yu-Jen Fang<sup>2,3,†</sup>, Riya Karmakar<sup>4</sup>, Arvind Mukundan<sup>4</sup> , Yu-Ming Tsao<sup>4</sup>, Chien-Wei Huang<sup>1,5,\*</sup> and Hsiang-Chen Wang<sup>4,6,7,\*</sup> 

- <sup>1</sup> Department of Medical Material Research, Kaohsiung Armed Forces General Hospital, 2, Zhongzheng 1st Rd., Lingya District, Kaohsiung City 80284, Taiwan; yangkaiyao@gmail.com
  - <sup>2</sup> Department of Internal Medicine, National Taiwan University Hospital, Yun-Lin Branch, No. 579, Sec. 2, Yunlin Rd., Dou-Liu 64041, Taiwan; toby851072@gmail.com
  - <sup>3</sup> Department of Internal Medicine, National Taiwan University College, No. 1 Jen Ai Rd. Sec. 1, Taipei 10051, Taiwan
  - <sup>4</sup> Department of Mechanical Engineering, National Chung Cheng University, 168, University Rd., Min Hsiung, Chiayi 62102, Taiwan; karmakarriya345@gmail.com (R.K.); d09420003@ccu.edu.tw (A.M.); d09420002@ccu.edu.tw (Y.-M.T.)
  - <sup>5</sup> Department of Nursing, Tajen University, 20, Weixin Rd., Yanpu Township, Pingtung 90741, Taiwan
  - <sup>6</sup> Department of Medical Research, Dalin Tzu Chi Hospital, Buddhist Tzu Chi Medical Foundation, No. 2, Minsheng Road, Dalin, Chiayi 62247, Taiwan
  - <sup>7</sup> Hitspectra Intelligent Technology Co., Ltd., 4F, No.2, Fuxing 4th Rd., Qianzhen District, Kaohsiung City 80661, Taiwan
- \* Correspondence: forevershiningfy@yahoo.com.tw (C.-W.H.); hcwang@ccu.edu.tw (H.-C.W.)  
† These authors contributed equally to this work.



**Citation:** Yang, K.-Y.; Fang, Y.-J.; Karmakar, R.; Mukundan, A.; Tsao, Y.-M.; Huang, C.-W.; Wang, H.-C. Assessment of Narrow Band Imaging Algorithm for Video Capsule Endoscopy Based on Decorrelated Color Space for Esophageal Cancer. *Cancers* **2023**, *15*, 4715. <https://doi.org/10.3390/cancers15194715>

Academic Editors: Hajime Isomoto, Michalis V. Karamouzis and Dimitrios Schizas

Received: 31 July 2023

Revised: 15 September 2023

Accepted: 24 September 2023

Published: 25 September 2023



**Copyright:** © 2023 by the authors. Licensee MDPI, Basel, Switzerland. This article is an open access article distributed under the terms and conditions of the Creative Commons Attribution (CC BY) license (<https://creativecommons.org/licenses/by/4.0/>).

**Simple Summary:** Video capsule endoscopy (VCE) is a small, patient-friendly tool used for medical imaging, but it lacks narrow band imaging (NBI), which is crucial for detecting various cancers like esophageal cancer (EC). EC is hard to detect early since it often shows no symptoms, leading to a low 5-year survival rate. NBI enhances mucosal features for early cancer identification, but adding it to VCE isn't feasible due to size constraints. This study successfully developed a method to convert traditional white light images (WLI) from VCE into NBI-like images for esophageal examination. The method performed well, with high similarity scores and improved image quality, offering a promising solution for better cancer detection.

**Abstract:** Video capsule endoscopy (VCE) is increasingly used to decrease discomfort among patients owing to its small size. However, VCE has a major drawback of not having narrow band imaging (NBI) functionality. The current VCE has the traditional white light imaging (WLI) only, which has poor performance in the computer-aided detection (CAD) of different types of cancer compared to NBI. Specific cancers, such as esophageal cancer (EC), do not exhibit any early biomarkers, making their early detection difficult. In most cases, the symptoms are unnoticeable, and EC is diagnosed only in later stages, making its 5-year survival rate below 20% on average. NBI filters provide particular wavelengths that increase the contrast and enhance certain features of the mucosa, thereby enabling early identification of EC. However, VCE does not have a slot for NBI functionality because its size cannot be increased. Hence, NBI image conversion from WLI can presently only be achieved in post-processing. In this study, a complete arithmetic assessment of the decorrelated color space was conducted to generate NBI images from WLI images for VCE of the esophagus. Three parameters, structural similarity index metric (SSIM), entropy, and peak-signal-to-noise ratio (PSNR), were used to assess the simulated NBI images. Results show the good performance of the NBI image reproduction method with SSIM, entropy difference, and PSNR values of 93.215%, 4.360, and 28.064 dB, respectively.

**Keywords:** narrow band imaging; hyperspectral imaging; decorrelated color space; video capsule endoscopy; peak-signal-to-noise ratio; structural similarity index metric; entropy

## 1. Introduction

Video capsule endoscopy (VCE) has been identified as a prospective substitute for traditional endoscopy in recent times [1], owing to the noninvasive nature of the device and its comparatively diminutive size [2–4]. The VCE device is designed to include a camera, a miniature lighting system, and an electronic box within its compact form factor, which is comparable in size to a tablet [5–7]. Despite its small size, VCE has the ability to generate high-quality images at a significantly higher frame rate [8,9]. Despite the numerous advantages of VCE, a significant drawback of this technology is its lack of narrow band imaging (NBI) functionality, which is commonly present in conventional endoscopes [10]. VCE relies solely on WLI, limiting its ability to detect subtle vascular patterns and mucosal details characteristic of NBI. Furthermore, VCE is prone to several other limitations such as its inability to perform therapeutic interventions, potential for capsule retention in cases of strictures, and challenges in localizing lesions precisely [11]. The exclusion of NBI from VCE means that subtle lesions, which may have crucial clinical implications, could be missed. Furthermore, VCE is a passive imaging modality incapable of therapeutic interventions or biopsies during the procedure, limiting its diagnostic scope and therapeutic utility.

NBI is a modality of medical imaging that employs a specialized filter to selectively permit the transmission of a specific wavelength of light [12,13]. The aforementioned wavelengths have the ability to enhance the contrast, thereby accentuating the features of the mucosal layer [14,15]. Typically, the central wavelength of NBI is either 415 or 540 nm, which correspond to the blue and green spectral bands, respectively [16,17]. The absorption of light by hemoglobin in the bloodstream is heightened at these particular wavelengths to provide enhanced precision, resulting in a darkened appearance of the blood vessels [18,19]. Consequently, the distinguishing features of the mucosa can be readily discerned from the neighboring milieu [20]. NBI bands are predominantly utilized in endoscopy for diagnosing diverse types of cancer [21].

The use of NBI in endoscopy is based on the principle that certain wavelengths of light can enhance the visualization of blood vessels and mucosal patterns in the gastrointestinal tract. Typically, NBI employs either a central wavelength of 415 nm (blue) or 540 nm (green) [22]. These specific wavelengths are chosen because they coincide with the absorption peaks of hemoglobin, the protein responsible for transporting oxygen in blood. Hemoglobin has two primary forms: oxygenated (oxyhemoglobin) and deoxygenated (deoxyhemoglobin). Oxyhemoglobin predominantly absorbs light in the blue spectrum, around 415 nm, whereas deoxyhemoglobin absorbs light in the green spectrum, around 540 nm [23]. When NBI light is directed onto the mucosal surface, it is preferentially absorbed by hemoglobin in blood vessels. This selective absorption results in a darkened appearance of blood vessels against a lighter background, greatly enhancing their visibility during endoscopic examination. This enhanced contrast and precision provided by NBI have proven invaluable in the detection of subtle mucosal changes, such as early neoplastic lesions and vascular patterns indicative of gastrointestinal pathology [24]. Consequently, NBI has become an essential tool in the early diagnosis and surveillance of gastrointestinal diseases.

Specific cancers, such as esophageal EC, which does not have any particular biomarker in early stages, can be diagnosed early with the use of NBI [21,25]. Many previous studies have proven that the accuracy, sensitivity, and specificity of early detection of various types of cancer increased significantly with the use of NBI [26–31]. Tsai et al. used single-shot detector and hyperspectral imaging to detect early EC and revealed that the overall accuracy of the NBI images was 91% and the RGB image's accuracy was only 88% [32]. Lee et al. examined EC by using the conventional white light imaging (WLI) and NBI, and concluded that NBI was much more effective than the conventional WLI in detecting

dysplasia [33]. Yosidha et al. demonstrated that the NBI system improved the accuracy of magnifying endoscopy [34]. Hence, the use of NBI is critical in VCE to detect early EC.

Therefore, in this study, the usability of NBI images simulated from decorrelated color spaces for VCE imaging of the esophagus was evaluated. The simulated NBI images were compared with three distinct parameters: PSNR, SSIM, and entropy. The narrow band conversion technology and the dataset employed in this study were discussed in depth. Subsequently, the outcomes obtained from the image comparison using various parameters were elucidated. Finally, a summary of the findings, the potential avenues for future research, and the limitations of this study were provided.

## 2. Materials and Methods

### 2.1. Dataset

Obtaining the necessary dataset for identifying and categorizing the esophagus can often be a challenging undertaking [35]. Moreover, a huge amount of pertinent information can be found in the VCE of the esophagus. In the present study, a series of esophageal images was obtained from two collaborating hospitals. The dataset consisted of a comprehensive collection of 3415 WLI VCE images of the esophagus. WLI images were obtained using VCE (InsightEyes EGD System, Insight Medical Solutions Inc., Hsinchu, Taiwan). VCE images of  $640 \times 480$  pixels in dimension were acquired from Taipei Veterans General Hospital. A supplementary set of 2000 WLI images obtained via a conventional endoscope (CV-290, Olympus, Shinjuku, Tokyo, Japan) was used for analysis. The dataset containing Olympus images was obtained from Chung-Ho Memorial Hospital at Kaohsiung Medical University. The dimension of these images was  $640 \times 480$  pixels.

### 2.2. NBI

The lack of NBI functionality is one of the most significant drawbacks associated with the use of VCE. Increasing the size of the VCE device is not possible because of the convenience factor. Therefore, the NBI features can be added only after the processing is completed. Given that NBI performs far more effectively with computer-aided detection machine learning techniques than WLI, this step is essential for early EC detection. Thus, in this study, a color space that replicated the NBI image was chosen to have decorrelated axes because it has been shown to be an effective tool for manipulating color images. The method developed by Reinhard et al. was applied [36]. Simply imposing the mean and standard deviation (SD) over the data points is a straightforward operation that, when combined with credible input images, results in the production of convincing output images. Only the mean and standard deviation in tandem with any of the three dimensions were needed in this investigation. Therefore, these metrics were calculated for the original image and the target image. A notable detail is that the average and standard deviation for each axis in one space were determined on an individual basis. First, a method that should be considered reasonable for converting RGB signals to l was demonstrated, the perception-based color space developed by Ruderman et al. [37] Considering l is a transform of LMS cone space, the image was converted to LMS space using the LMS transform in two steps. First, the RGB tristimulus values were converted to XYZ ones. By using the standard matrix provided by the International Telecommunications Union, a vector that can be applied to multiply the columns was obtained, resulting in the RGB-to-XYZ conversion. The image was converted for it to be in LMS space using the traditional conversion matrix, as shown in Equation (1).

$$\begin{pmatrix} L \\ M \\ S \end{pmatrix} = \begin{pmatrix} 0.3811 & 0.5783 & 0.0402 \\ 0.1967 & 0.7244 & 0.0782 \\ 0.0241 & 0.1288 & 0.8444 \end{pmatrix} \cdot \begin{pmatrix} R \\ G \\ B \end{pmatrix} \quad (1)$$

The information in this color space exhibited a significant amount of skew, which was reduced to a significant degree after transforming the data to the logarithmic space, as shown in Equation (2).

$$L = \log LM = \log MS = \log S \quad (2)$$

First, the data points were taken, and the mean was subtracted from them. Then, the data points that made up the synthetic image were adjusted using the factors determined by the standard deviations of each of the individual data points, as shown in Equation (3).

$$l' = \frac{\sigma_t^l}{\sigma_s^l} l^* \alpha' = \frac{\sigma_t^\alpha}{\sigma_s^\alpha} \alpha^* \beta' = \frac{\sigma_t^\beta}{\sigma_s^\beta} \beta^* \quad (3)$$

Choosing a source image and a target image that do not go together very well is possible because this investigation aimed to copy the appearance of one image onto another. The compositional similarities between the images can determine the quality of the final product. For instance, if the synthetic image has a significant amount of grass, whereas the photograph has a great amount of sky, then the transformation of statistics could be assumed to be unsuccessful.

### 2.3. Parameters for Comparison

#### 2.3.1. SSIM

SSIM is a widely recognized quality measurement that is utilized in the process of determining how similar two images are to one another [38]. It was introduced by Wang et al., and it has been proposed to be associated with the human visual system's quality perception [39]. SSIM is developed by predicting every image distortion as an amalgamation of three factors, loss of correlation, contrast distortion, and luminance distortion, rather than using traditional error summation methods [40,41]. SSIM is used as a measure to compare the similarity between WLI Images and NBI images [42]. SSIM metric has gained significant popularity in the field of digital image analysis due to its ease of use, widespread application, and established validity through rigorous testing [43,44]. SSIM values usually range between 0 and 100%, and SSIM values of more than 90% are considered better results [45].

#### 2.3.2. Entropy

The second criterion employed to assess the algorithm formulated in this investigation was entropy [46]. The calculation of entropy was similar to that of SSIM. The entropy discrepancy between the WLI images acquired through the Olympus endoscope and the simulated NBI images was compared. Entropy can be utilized in image processing for the purpose of texture classification. A specific texture may exhibit a distinct entropy value because certain patterns tend to recur in a relatively consistent manner [47]. Within the framework of the paper, low entropy is indicative of reduced disorder and diminished variance among the constituent elements. Thus, reducing the entropy results in an improved reproduction of the image. The entropy disparity between the WLI images acquired through VCE and the simulated NBI images was compared.

#### 2.3.3. PSNR

PSNR is a byte-by-byte comparison of the quality of two images [48,49]. It is one of the simplest methods to compare the source and the reproduced image [50]. PSNR is analyzed similar to SSIM. The corresponding WLI images from VCE and the Olympus endoscope were separately compared with the simulated NBI images. PSNR values range between 20 and 60 dB, and the higher the value is, the better the result. For an 8-bit data representation, the accepted PSNR value is about 25 dB [51].

## 3. Results

In this study, three important parameters were considered for analyzing the effectiveness of the algorithm: PSNR, SSIM, and entropy. Comparing the results of these parameters can help understand the limitations and advantages of the proposed method.

### 3.1. SSIM

Figure 1 shows the results of the SSIM analysis. The SSIM value lies in the range of 0 to 100%, with a higher value indicating a better result. In this study, 50 random WLI images and their corresponding simulated NBI images were compared to compare the SSIM between the WLI images and the simulated NBI images. The average SSIM values for the Olympus and VCE images were 90% and 92.49%, respectively. However, out of the 50 images, 21 VCE images had a high SSIM of more than 93%. Out of the 50 randomly selected images, 19 had an SSIM of 91%, and only nine images had less than 84% (Supplementary Table S3). These findings revealed that the average SSIM decreased because of these nine images. These images were either blurred, had too much light reflected on them, or had some flare. Therefore, the SSIM value decreased below 91%. If the dataset was filtered and had a clearer WLI, then the NBI reproduction of the images could be better. Similar to the Olympus images, the eight WLI images in VCE had considerable reflection that made the SSIM value less than 90%. However, in all the different conditions, the SSIM values did not reduce to below 90% in VCE. Therefore, regardless of the errors present in the image, the NBI reproduction can be profound.

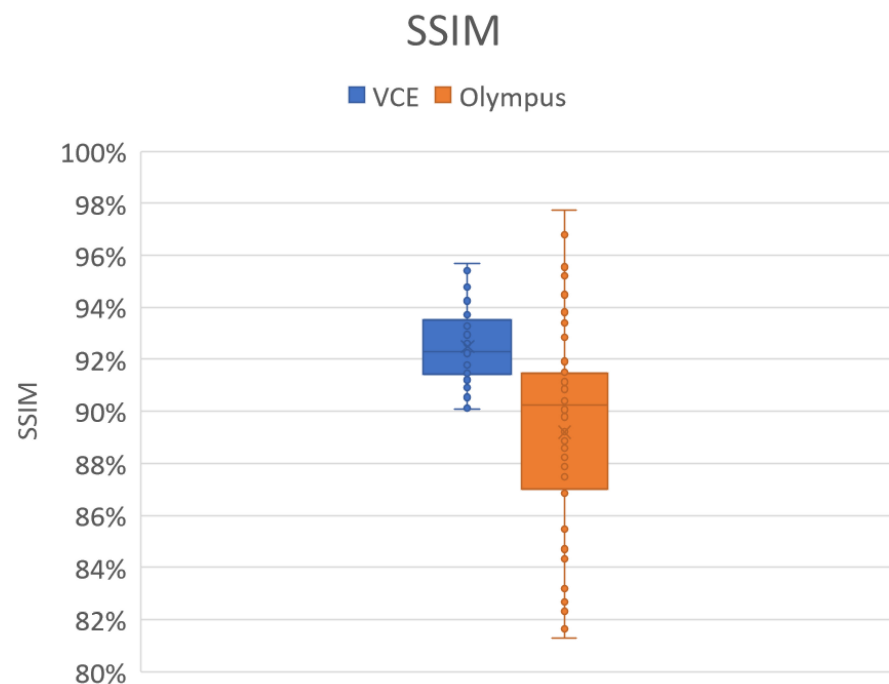


**Figure 1.** SSIM metric of 50 random Olympus and VCE images.

### 3.2. Entropy

The entropy difference between the Olympus endoscope and VCE is illustrated in Figure 2. The average entropy difference between the WLI and simulated NBI images in VCE was around 2.6942%, and average entropy difference between the WLI and simulated images from the Olympus endoscope was 2.3457% (Supplementary Table S2). The results showed that the entropy in the Olympus endoscope and VCE followed a similar pattern: when the entropy increased in the WLI images, the entropy of the NBI images also increased, and vice versa. In VCE and the Olympus endoscope, the entropy in the NBI images increased because of three images (image numbers 20, 25, and 46). This finding can be attributed to the excessive reflection seen in the WLI image, indicating the successful utilization of the algorithm in this study. The differences in entropy between images provide insight into the levels of randomness or disorder present in the pixel intensity values within each image. Entropy differences between the same images can indicate variations in information content or randomness within the images. Higher entropy differences suggest greater dissimilarity between the images, potentially due to noise, compression artifacts,

or alterations. Conversely, lower entropy differences imply more similarity or consistency between the images, indicating minimal changes or distortions. Analyzing these differences can be useful in quality control, image restoration, or change detection applications, helping identify and quantify the extent of image alterations or discrepancies and ultimately aiding in image analysis and processing tasks.

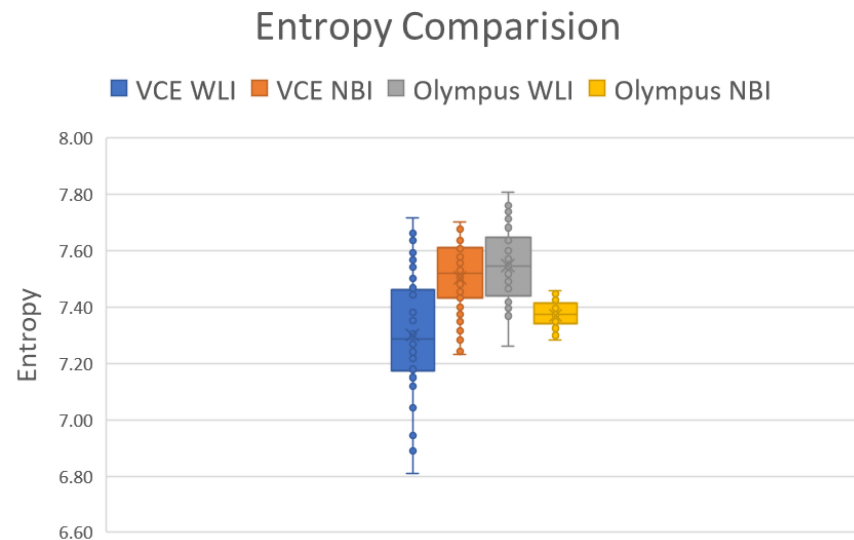


**Figure 2.** Entropy of 50 randomly chosen Olympus and VCE images.

### 3.3. PSNR

Figure 3 shows the PSNR value of the 50 randomly chosen VCE and Olympus endoscopic images. The average PSNR values of the VCE and Olympus endoscopic images were 27.8212 and 28.0813 dB, respectively (Supplementary Table S1). The results of SSIM, entropy, and PSNR showed that the proposed algorithm performed better.

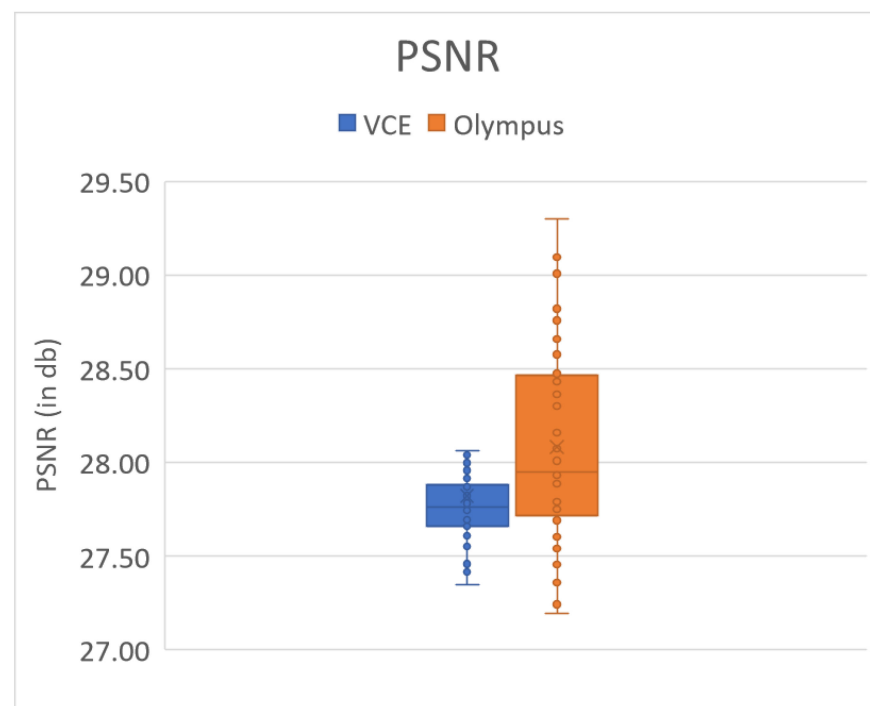


**Figure 3.** PSNR comparison of 50 randomly chosen Olympus and VCE images.

#### 4. Discussion

In this study, a decolored axis color-matching function was used to simulate NBI images from the VCE WLI images by using the NBI image from an Olympus endoscope as a reference. Given that VCE is more preferred than the traditional endoscopy, incorporating NBI capability onto VCE is an important requisite because VCE does not currently have NBI functionality. Such functionality has been proven to be more effective in detecting early cancer cells, specifically EC, which does not have any early biomarkers. This incorporation could increase the 5-year survival rate of EC drastically. The results of this study showed that the reproduced NBI images had better comparison metric values. First, the average SSIM values of the Olympus and VCE endoscopic images were 89.1995% and 92.4919%, respectively. Second, the average entropy values of the randomly chosen WLI images and their corresponding NBI images in VCE and the Olympus endoscope were 2.6942% and 2.3457%, respectively. Finally, the PSNRs of the WLI images and their corresponding NBI images in VCE and the Olympus endoscope were 27.8212 and 28.0813 dB, respectively. The future scope of this study is to test the reproduced NBI images with a YOLOv5 deep learning model with a dataset of EC to detect and classify cancers on the basis of stage severity. Then, the same model could be used to compare the accuracy, sensitivity, and specificity of WLI of those NBI. However, one of the limitations of this method is that it did not consider the lighting spectrum of the WLI and NBI images. Therefore, if the WLI image is blurred or has light reflections on it, the NBI image could not be a perfect simulation. The simulated NBI image with the corresponding WLI of the VCE endoscope is shown in Figure 4 (Supplementary Figure S1 shows 50 randomly chosen images of WLI in VCE, and Figure S2 shows 50 randomly chosen images of the simulated NBI in VCE). The simulated NBI image with the corresponding WLI and a similar NBI image from the Olympus endoscope are shown in Figure 5 (Supplementary Figure S3 shows six randomly chosen images of WLI in VCE, and Figures S3 and S4 shows another 12 randomly chosen images of simulated NBI in VCE).

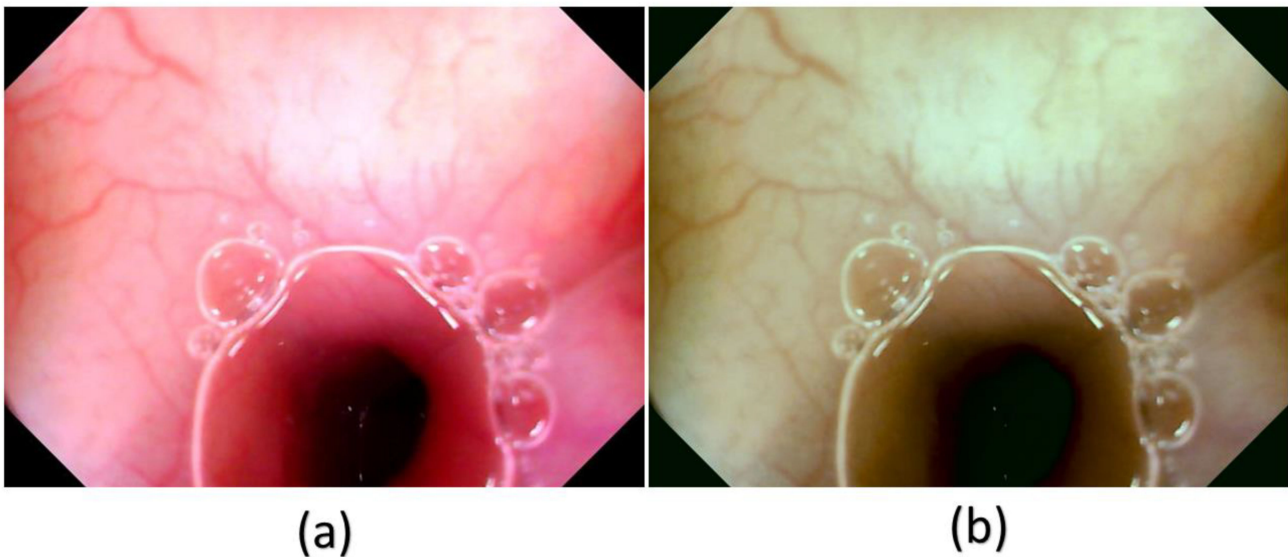


**Figure 4.** Comparison between WLI and simulated NBI images of VCE. (a) WLI image from VCE, (b) simulated NBI image from the NBI conversion algorithm.

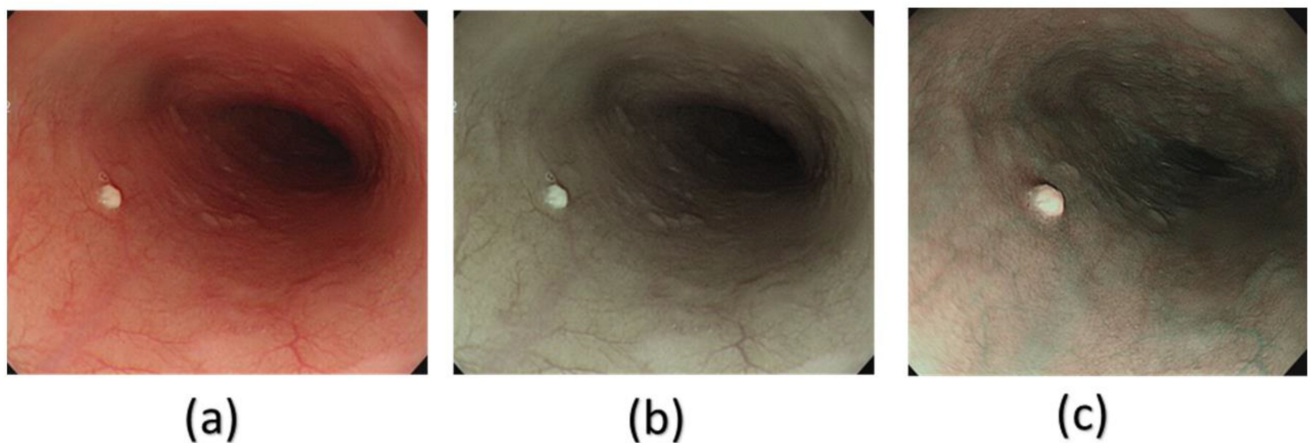


**Figure 5.** Comparison among the (a) WLI images, (b) simulated NBI images, and (c) real NBI images from the Olympus endoscope.

## 5. Conclusions

In this study, a decolored axis color-matching function was implemented to simulate NBI images from VCE WLI images by making use of the NBI image obtained from an Olympus endoscope as a reference. VCE does not currently have NBI functionality, which has been proven to be more effective in detecting early cancer cells, particularly early EC, which does not have any early biomarkers. Given that VCE is more preferred than the traditional endoscopy, incorporating NBI capability into VCE is an important requisite that could result in a significant increase in the 5-year survival rate of patients with EC. The results showed that the reproduced NBI images had higher comparison metric values. The images from the Olympus endoscope and VCE had average SSIM values of 98.415% and 93.215%, respectively. The random WLI images and their corresponding NBI images obtained from VCE and the Olympus endoscopes showed average entropy values of 3.45% and 4.36%, respectively. The PSNRs of the WLI images with their corresponding NBI images in VCE and the Olympus endoscope were 28.06 and 28.15%, respectively.

**Supplementary Materials:** The following supporting information can be downloaded at <https://www.mdpi.com/article/10.3390/cancers15194715/s1>, Table S1: Results of PSNR comparison of each image in Olympus and VCE; Table S2: Results of Entropy comparison of each image in Olympus and VCE; Table S3: Results of SSIM comparison of each image in Olympus and VCE; Figure S1: 50 Randomly chosen images of WLI in VCE; Figure S2: 50 Randomly chosen images of NBI in VCE; Figure S3: 6 Randomly chosen WLI images, simulated NBI images and a similar original NBI in Olympus endoscope. (a) Olympus WLI images. (b) simulated NBI image and (c) a similar NBI image from Olympus; Figure S4: 6 Randomly chosen WLI images, simulated NBI images and a similar original NBI in Olympus endoscope. (a) Olympus WLI images. (b) simulated NBI image and (c) a similar NBI image from Olympus.

**Author Contributions:** Conceptualization, K.-Y.Y., H.-C.W. and A.M.; data curation, K.-Y.Y., Y.-M.T. and A.M.; formal analysis, K.-Y.Y., R.K. and A.M.; funding acquisition, C.-W.H., Y.-J.F. and H.-C.W.; investigation, R.K., Y.-M.T. and A.M.; methodology, Y.-J.F., H.-C.W. and A.M.; project administration, Y.-M.T., A.M. and H.-C.W.; resources, C.-W.H., H.-C.W. and A.M.; software, Y.-M.T. and A.M.; supervision, C.-W.H., Y.-M.T. and H.-C.W.; validation, Y.-J.F., Y.-M.T. and A.M.; writing—original draft, R.K. and A.M.; writing—review and editing, R.K., A.M. and H.-C.W. All authors have read and agreed to the published version of the manuscript.

**Funding:** This research was supported by National Science and Technology Council, the Republic of China under grants NSTC 112-2221-E-194-036. This work was financially or partially supported by the National Chung Cheng University-National Taiwan University Hospital Yunlin Branch Joint Research Program (CCU-NTUHYB-112-NC002), National Taiwan University Hospital Yunlin Branch (112-C001) and Kaohsiung Armed Forces General Hospital research project 112-010 in Taiwan.

**Institutional Review Board Statement:** The study was conducted by the guidelines of the Declaration of Helsinki and approved by the Institutional Review Board of National Taiwan University Hospital (NTUH) (NTUH-202009096RIND) and the Institutional Review Board of Kaohsiung Armed Forces General Hospital (KAFGHIRB 112-018).

**Informed Consent Statement:** Written informed consent was waived in this study because of the retrospective, anonymized nature of study design.

**Data Availability Statement:** The data presented in this study are available in this article upon request to the corresponding author.

**Conflicts of Interest:** The authors declare no conflict of interest.

## References

1. Sahafi, A.; Wang, Y.; Rasmussen, C.; Bollen, P.; Baatrup, G.; Blanes-Vidal, V.; Herp, J.; Nadimi, E. Edge artificial intelligence wireless video capsule endoscopy. *Sci. Rep.* **2022**, *12*, 13723. [[CrossRef](#)]
2. Ding, Z.; Wang, W.; Zhang, K.; Ming, F.; Yangdai, T.; Xu, T.; Shi, H.; Bao, Y.; Yao, H.; Peng, H. Novel scheme for non-invasive gut bioinformation acquisition with a magnetically controlled sampling capsule endoscope. *Gut* **2021**, *70*, 2297–2306. [[CrossRef](#)]
3. Hosoe, N.; Takabayashi, K.; Ogata, H.; Kanai, T. Capsule endoscopy for small-intestinal disorders: Current status. *Dig. Endosc.* **2019**, *31*, 498–507. [[CrossRef](#)]
4. Vasilakakis, M.; Koulaouzidis, A.; Marlicz, W.; Iakovidis, D. The future of capsule endoscopy in clinical practice: From diagnostic to therapeutic experimental prototype capsules. *Gastroenterol. Rev. Przegląd Gastroenterol.* **2020**, *15*, 179–193. [[CrossRef](#)]
5. Noormohammadi, R.; Khaleghi, A.; Balasingham, I. Battery-free wireless communication for video capsule endoscopy. In Proceedings of the 2019 13th International Symposium on Medical Information and Communication Technology (ISMICT), Oslo, Norway, 8–10 May 2019; pp. 1–5.
6. Vedaei, S.S.; Wahid, K.A. A localization method for wireless capsule endoscopy using side wall cameras and IMU sensor. *Sci. Rep.* **2021**, *11*, 11204. [[CrossRef](#)]
7. Duan, Z.; Xu, L.-J.; Gao, S.; Geyi, W. Integrated design of wideband omnidirectional antenna and electronic components for wireless capsule endoscopy systems. *IEEE Access* **2018**, *6*, 29626–29636. [[CrossRef](#)]
8. Jang, J.; Lee, J.; Lee, K.-R.; Lee, J.; Kim, M.; Lee, Y.; Bae, J.; Yoo, H.-J. 4-Camera VGA-resolution capsule endoscope with 80Mb/s body-channel communication transceiver and Sub-cm range capsule localization. In Proceedings of the 2018 IEEE International Solid-State Circuits Conference (ISSCC), San Francisco, CA, USA, 11–15 February 2018; pp. 282–284.
9. Almalioglu, Y.; Ozyoruk, K.B.; Gokce, A.; Incetan, K.; Gokceler, G.I.; Simsek, M.A.; Ararat, K.; Chen, R.J.; Durr, N.J.; Mahmood, F. EndoL2H: Deep super-resolution for capsule endoscopy. *IEEE Trans. Med. Imaging* **2020**, *39*, 4297–4309. [[CrossRef](#)]
10. Yen, C.-T.; Lai, Z.-W.; Lin, Y.-T.; Cheng, H.-C. Optical design with narrow-band imaging for a capsule endoscope. *J. Healthc. Eng.* **2018**, *2018*, 5830759. [[CrossRef](#)]
11. Marmo, R.; Rotondano, G.; Piscopo, R.; Bianco, M.A.; Siani, A.; Catalano, O.; Cipolletta, L. Capsule endoscopy versus enteroclysis in the detection of small-bowel involvement in Crohn's disease: A prospective trial. *Clin. Gastroenterol. Hepatol.* **2005**, *3*, 772–776. [[CrossRef](#)]
12. Sano, Y.; Tanaka, S.; Kudo, S.e.; Saito, S.; Matsuda, T.; Wada, Y.; Fujii, T.; Ikematsu, H.; Uraoka, T.; Kobayashi, N. Narrow-band imaging (NBI) magnifying endoscopic classification of colorectal tumors proposed by the Japan NBI Expert Team. *Dig. Endosc.* **2016**, *28*, 526–533. [[CrossRef](#)]
13. Sun, C.; Han, X.; Li, X.; Zhang, Y.; Du, X. Diagnostic performance of narrow band imaging for laryngeal cancer: A systematic review and meta-analysis. *Otolaryngol. –Head Neck Surg.* **2017**, *156*, 589–597. [[CrossRef](#)]
14. Vu, A.; Farah, C.S. Narrow band imaging: Clinical applications in oral and oropharyngeal cancer. *Oral Dis.* **2016**, *22*, 383–390. [[CrossRef](#)]
15. Aloisi, A.; Sonoda, Y.; Gardner, G.J.; Park, K.J.; Elliott, S.L.; Zhou, Q.C.; Iasonos, A.; Abu-Rustum, N.R. Prospective comparative study of laparoscopic narrow band imaging (NBI) versus standard imaging in gynecologic oncology. *Ann. Surg. Oncol.* **2018**, *25*, 984–990. [[CrossRef](#)]
16. Silva, M.F.; Rodrigues, J.A.; Ghaderi, M.; Goncalves, L.M.; De Graaf, G.; Wolffenbuttel, R.F.; Correia, J.H. NBI optical filters in minimally invasive medical devices. *IEEE J. Sel. Top. Quantum Electron.* **2016**, *22*, 165–171. [[CrossRef](#)]
17. Kimza, H.; Jackowska, J.; Wierzbicka, M. The usefulness of the NBI-narrow band imaging for the larynx assessment. *Pol. J. Otolaryngol.* **2018**, *72*, 1–3. [[CrossRef](#)]
18. White, J.R.; Sami, S.S.; Reddiar, D.; Mannath, J.; Ortiz-Fernández-Sordo, J.; Beg, S.; Scott, R.; Thiagarajan, P.; Ahmad, S.; Parra-Blanco, A. Narrow band imaging and serology in the assessment of premalignant gastric pathology. *Scand. J. Gastroenterol.* **2018**, *53*, 1611–1618. [[CrossRef](#)]
19. Wisotzky, E.L.; Uecker, F.C.; Arens, P.; Dommerich, S.; Hilsmann, A.; Eisert, P. Intraoperative hyperspectral determination of human tissue properties. *J. Biomed. Opt.* **2018**, *23*, 091409. [[CrossRef](#)]
20. Zhou, F.; Wu, L.; Huang, M.; Jin, Q.; Qin, Y.; Chen, J. The accuracy of magnifying narrow band imaging (ME-NBI) in distinguishing between cancerous and noncancerous gastric lesions: A meta-analysis. *Medicine* **2018**, *97*, 5851730. [[CrossRef](#)]

21. Tsai, T.-J.; Mukundan, A.; Chi, Y.-S.; Tsao, Y.-M.; Wang, Y.-K.; Chen, T.-H.; Wu, I.-C.; Huang, C.-W.; Wang, H.-C. Intelligent Identification of Early Esophageal Cancer by Band-Selective Hyperspectral Imaging. *Cancers* **2022**, *14*, 4292. [[CrossRef](#)]
22. Gono, K.; Obi, T.; Yamaguchi, M.; Ohyama, N.; Machida, H.; Sano, Y.; Yoshida, S.; Hamamoto, Y.; Endo, T. Appearance of enhanced tissue features in narrow-band endoscopic imaging. *J. Biomed. Opt.* **2004**, *9*, 568–577. [[CrossRef](#)]
23. Piazza, C.; Dessouky, O.; Peretti, G.; Cocco, D.; De Benedetto, L.; Nicolai, P. Narrow-band imaging: A new tool for evaluation of head and neck squamous cell carcinomas. Review of the literature. *Acta Otorhinolaryngol. Ital.* **2008**, *28*, 49. [[PubMed](#)]
24. Pasha, S.F.; Leighton, J.A.; Das, A.; Gurudu, S.; Sharma, V.K. Narrow band imaging (NBI) and white light endoscopy (WLE) have a comparable yield for detection of colon polyps in patients undergoing screening or surveillance colonoscopy: A meta-analysis. *Gastrointest. Endosc.* **2009**, *69*, AB363. [[CrossRef](#)]
25. Fang, Y.-J.; Mukundan, A.; Tsao, Y.-M.; Huang, C.-W.; Wang, H.-C. Identification of Early Esophageal Cancer by Semantic Segmentation. *J. Pers. Med.* **2022**, *12*, 1204. [[CrossRef](#)] [[PubMed](#)]
26. Puvanakrishnan, P.; Diagaradjane, P.; Kazmi, S.S.; Dunn, A.K.; Krishnan, S.; Tunnell, J.W. Narrow band imaging of squamous cell carcinoma tumors using topically delivered anti-EGFR antibody conjugated gold nanorods. *Lasers Surg. Med.* **2012**, *44*, 310–317. [[CrossRef](#)]
27. Tan, N.C.-W.; Herd, M.K.; Brennan, P.A.; Puxeddu, R. The role of narrow band imaging in early detection of head and neck cancer. *Br. J. Oral Maxillofac. Surg.* **2012**, *50*, 132–136. [[CrossRef](#)]
28. Watanabe, A.; Taniguchi, M.; Tsujie, H.; Hosokawa, M.; Fujita, M.; Sasaki, S. The value of narrow band imaging for early detection of laryngeal cancer. *Eur. Arch. Oto-Rhino-Laryngol.* **2009**, *266*, 1017–1023. [[CrossRef](#)]
29. Wang, S.; Zhang, Y.; Dong, Z.; Du, S.; Ji, G.; Yan, J.; Yang, J.; Wang, Q.; Feng, C.; Phillips, P. Feed-forward neural network optimized by hybridization of PSO and ABC for abnormal brain detection. *Int. J. Imaging Syst. Technol.* **2015**, *25*, 153–164. [[CrossRef](#)]
30. Zhang, Y.; Wang, S.; Sui, Y.; Yang, M.; Liu, B.; Cheng, H.; Sun, J.; Jia, W.; Phillips, P.; Gorriz, J.M. Multivariate approach for Alzheimer’s disease detection using stationary wavelet entropy and predator-prey particle swarm optimization. *J. Alzheimer’s Dis.* **2018**, *65*, 855–869. [[CrossRef](#)]
31. Zhang, Y.-D.; Zhao, G.; Sun, J.; Wu, X.; Wang, Z.-H.; Liu, H.-M.; Govindaraj, V.V.; Zhan, T.; Li, J. Smart pathological brain detection by synthetic minority oversampling technique, extreme learning machine, and Jaya algorithm. *Multimed. Tools Appl.* **2018**, *77*, 22629–22648. [[CrossRef](#)]
32. Tsai, C.-L.; Mukundan, A.; Chung, C.-S.; Chen, Y.-H.; Wang, Y.-K.; Chen, T.-H.; Tseng, Y.-S.; Huang, C.-W.; Wu, I.-C.; Wang, H.-C. Hyperspectral Imaging Combined with Artificial Intelligence in the Early Detection of Esophageal Cancer. *Cancers* **2021**, *13*, 4593. [[CrossRef](#)]
33. Lee, C.; Chang, C.; Lee, Y.; Tai, C.; Wang, W.; Tseng, P.-H.; Hwang, J.; Hwang, T.; Wang, C.; Lin, J. Narrow-band imaging with magnifying endoscopy for the screening of esophageal cancer in patients with primary head and neck cancers. *Endoscopy* **2010**, *42*, 613–619. [[CrossRef](#)] [[PubMed](#)]
34. Yoshida, T.; Inoue, H.; Usui, S.; Satodate, H.; Fukami, N.; Kudo, S.-e. Narrow-band imaging system with magnifying endoscopy for superficial esophageal lesions. *Gastrointest. Endosc.* **2004**, *59*, 288–295. [[CrossRef](#)] [[PubMed](#)]
35. Thamir, N.N.; Mohammed, F.G. Early Esophageal Cancer detection using Deep learning Techniques. *J. Phys. Conf. Ser.* **2021**, *1963*, 012066. [[CrossRef](#)]
36. Reinhard, E.; Adhikhmin, M.; Gooch, B.; Shirley, P. Color transfer between images. *IEEE Comput. Graph. Appl.* **2001**, *21*, 34–41. [[CrossRef](#)]
37. Ruderman, D.L.; Cronin, T.W.; Chiao, C.C. Statistics of Cone Responses to Natural Images: Implications for Visual Coding. *J. Opt. Soc. Am.* **1998**, *15*, 2036–2045. [[CrossRef](#)]
38. Brunet, D.; Vrscay, E.R.; Wang, Z. On the mathematical properties of the structural similarity index. *IEEE Trans. Image Process.* **2011**, *21*, 1488–1499. [[CrossRef](#)]
39. Wang, Z.; Bovik, A.C.; Sheikh, H.R.; Simoncelli, E.P. Image quality assessment: From error visibility to structural similarity. *IEEE Trans. Image Process.* **2004**, *13*, 600–612. [[CrossRef](#)]
40. Hore, A.; Ziou, D. Image quality metrics: PSNR vs. SSIM. In Proceedings of the 2010 20th International Conference on Pattern Recognition, Istanbul, Turkey, 23–26 August 2010; pp. 2366–2369.
41. Dosselmann, R.; Yang, X.D. A comprehensive assessment of the structural similarity index. *Signal Image Video Process.* **2011**, *5*, 81–91. [[CrossRef](#)]
42. Sara, U.; Akter, M.; Uddin, M.S. Image quality assessment through FSIM, SSIM, MSE and PSNR—A comparative study. *J. Comput. Commun.* **2019**, *7*, 8–18. [[CrossRef](#)]
43. Setiadi, D.R.I.M. PSNR vs SSIM: Imperceptibility quality assessment for image steganography. *Multimed. Tools Appl.* **2021**, *80*, 8423–8444. [[CrossRef](#)]
44. Ndajah, P.; Kikuchi, H.; Yukawa, M.; Watanabe, H.; Muramatsu, S. SSIM image quality metric for denoised images. In Proceedings of the 3rd WSEAS International Conference on Visualization, Imaging and Simulation, Faro, Portugal, 3–5 November 2010; pp. 53–58.
45. Nilsson, J.; Akenine-Möller, T. Understanding ssim. *arXiv* **2020**, arXiv:2006.13846.
46. Tsai, D.-Y.; Lee, Y.; Matsuyama, E. Information Entropy Measure for Evaluation of Image Quality. *J. Digit. Imaging* **2008**, *21*, 338–347. [[CrossRef](#)] [[PubMed](#)]
47. Pal, N.R.; Pal, S.K. Entropy: A new definition and its applications. *IEEE Trans. Syst. Man Cybern.* **1991**, *21*, 1260–1270. [[CrossRef](#)]

48. Winkler, S.; Mohandas, P. The Evolution of Video Quality Measurement: From PSNR to Hybrid Metrics. *IEEE Trans. Broadcast.* **2008**, *54*, 660–668. [[CrossRef](#)]
49. Huynh-Thu, Q.; Ghanbari, M. The accuracy of PSNR in predicting video quality for different video scenes and frame rates. *Telecommun. Syst.* **2012**, *49*, 35–48. [[CrossRef](#)]
50. Tanchenko, A. Visual-PSNR measure of image quality. *J. Vis. Commun. Image Represent.* **2014**, *25*, 874–878. [[CrossRef](#)]
51. Deshpande, R.G.; Raha, L.L.; Sharma, S.K. Video quality assessment through psnr estimation for different compression standards. *Indones. J. Electr. Eng. Comput. Sci.* **2018**, *11*, 918–924. [[CrossRef](#)]

**Disclaimer/Publisher’s Note:** The statements, opinions and data contained in all publications are solely those of the individual author(s) and contributor(s) and not of MDPI and/or the editor(s). MDPI and/or the editor(s) disclaim responsibility for any injury to people or property resulting from any ideas, methods, instructions or products referred to in the content.